Use of Drone LIDAR Scanning for Volume Estimation of Stockpiles Accumulated in Post-Flotation Sedimentation Ponds – A Case Study of Bukowno (Southern Poland)

Ireneusz Laks[1*)], Krzysztof Achtenberg[2)]

[1*)]Poznan University of Life Sciences, ul. Wojska Polskiego 28, 60-623 Poznan, Poland; ireneusz.laks@up.poznan.pl; ORCID: 0000-0003-4078-9600
[2)]Poznan University of Life Sciences, ul. Wojska Polskiego 28, 60-623 Poznan, Poland; krzysztof.achtenberg@up.poznan.pl; ORCID: 0000-0001-8675-2972

https://doi.org/10.29227/IM-2025-02-02-032

Submission date: *2025-08-11* | Review date: *2025-08-29*

Abstract

This study evaluates the use of drone-mounted LiDAR scanning to estimate the volume of post-flotation tailings accumulated in sedimentation ponds located in Bukowno, southern Poland. The survey was conducted using a DJI Matrice 350 RTK UAV equipped with the Zenmuse L2 LiDAR sensor, supported by high-accuracy GNSS measurements using the Topcon HiPer XR receiver. The main goal was to generate a high-resolution 3D model of the tailings storage area and assess the geometric accuracy of horizontal and vertical geodetic coordinates using control points and statistical validation. Post-processing of LiDAR data was performed using DJI Terra, followed by spatial and statistical analyses in QGIS and RStudio. Statistical evaluation included descriptive statistics, Tukey's outlier detection, and the Shapiro–Wilk test to verify the normality of error distributions. The horizontal accuracy was assessed using 10 control points, while the vertical accuracy relied on 46 measured control points. The analysis confirmed the high accuracy of the generated model, with average absolute elevation error not exceeding 1.7 cm and horizontal deviations ranging from 1.7 cm (Δx) to 3.6 cm (Δy). The volume of deposited tailings above the reference elevation of 320.00 m a.s.l. was calculated to be 37.49 million m³ over an area of 137.9 hectares. The Eastern pond was further divided into operational subsections to support functional assessment and monitoring strategies.

Keywords: DLS, L2 LiDAR, 3D model, error estimation, post-flotation sed

1. Introduction

Reliable information about engineering structures that significantly affect the natural environment is essential for ensuring safety, effective management, and environmental protection. Among these, post-flotation sedimentation ponds represent particularly critical sites due to the nature and volume of deposited industrial waste. In Poland, the Żelazny Most reservoir, owned by KGHM Polska Miedź S.A., is not only the largest facility of this kind in Europe but also one of the largest worldwide. Another notable example is the Bukowno sedimentation ponds, located in southern Poland, which accumulate post-flotation residues from secondary zinc ore processing. Accurate knowledge of the volume and characteristics of stored sediments, as well as regular monitoring of the structural layout of the site—such as embankment geometry, slope formation, and access roads—is crucial for both facility operators and environmental regulatory agencies.

While traditional geodetic surveys provide essential updates during ongoing works, they are often time-consuming and yield only simplified geometric representations of these complex structures. For a comprehensive understanding of such sites, the use of advanced remote sensing technologies, especially aerial laser scanning (LiDAR), becomes indispensable. These methods enable the high-resolution 3D reconstruction of the entire sedimentation pond, including detailed information on terrain morphology, sediment volumes, and even vegetation cover—differentiated by type. Integrating such detailed spatial datasets into monitoring routines allows for improved environmental oversight, structural maintenance, and informed decision-making regarding long-term management, rehabilitation, or closure of such facilities.

LiDAR (Light Detection and Ranging) is a remote sensing method that uses laser pulses to measure distances to the Earth's surface. Mounted on aerial platforms such as drones or airplanes, LiDAR sensors can collect high-density point cloud data used to generate precise 3D terrain models. A notable advancement in this technology is the Zenmuse L2 LiDAR sensor by DJI, which integrates with RTK/PPK GNSS systems and a high-precision IMU, enabling sub-decimeter vertical accuracy in suitable conditions.

Most researchers and engineers [1,2,3] emphasize the considerable advantages of UAV-mounted LiDAR systems in geospatial, engineering, and environmental applications. LiDAR sensors deployed on drones are capable of generating extremely high-density point clouds—often exceeding 1,000 points per square meter—which allow for the development of highly detailed Digital Terrain Models (DTMs), Digital Elevation Models (DEMs), and Canopy Height Models (CHMs). These capabilities are particularly valuable for applications involving change detection, erosion monitoring, hydrological modeling, and vegetation analysis.

MacDonell et al.[4] evaluated the performance of a consumer-grade UAV-mounted solid-state LiDAR system, specifically the DJI Zenmuse L1 sensor mounted on a Matrice 300 RTK drone, for topographic surveying in moderately vegetated fluvial environments. The study systematically examined the influence of varying flight parameters (altitude and velocity) on the accuracy and density of the resulting elevation models. Results indicated minimal georeferencing errors across flight profiles, with vertical root mean square errors (RMSE) typically under 10 cm. These findings underscore the reliability and cost-efficiency of such systems for high-resolution terrain modeling, even in conditions with moderate vegetation cover.

Similarly, Resop et al.[5] conducted a comparative study between Drone Laser Scanning (DLS) and traditional Airborne Laser Scanning (ALS) for riverscape mapping. Their case study focused on Stroubles Creek in Virginia, USA, and demonstrated that DLS offered superior

resolution and vegetation classification, particularly in capturing fine-scale channel morphology and detecting low-lying vegetation. These advantages are critical in stream restoration design, riparian habitat assessment, and hydrological simulation. The authors also emphasized that DLS systems significantly reduce scan shadowing at lower altitudes and enhance return rates in densely vegetated areas—limitations often encountered with ALS.

Both studies highlighted the robustness of DJI's solid-state LiDAR technology, which delivered consistent and accurate topographic data with limited post-processing complications. Processing workflows commonly included the use of software tools such as DJI Terra, Terrasolid, and QGIS for point cloud georeferencing, noise filtering, classification into ground and non-ground classes, and the generation of usable 3D surface models. The ability to quickly classify ground surfaces and vegetation layers—often aided by semi-automated or AI-supported algorithms—makes UAV-LiDAR an essential tool in modern geomatics and environmental monitoring.

In conclusion, UAV-based LiDAR systems offer a compelling alternative to traditional survey methods, balancing precision, resolution, and operational flexibility. Their growing use in industrial zones, floodplains, and river valleys reflects the increasing demand for rapid, high-fidelity topographic data for a wide range of scientific and engineering applications.

The application of LiDAR technology for earth mass analysis on various types of storage sites—such as mining tailings ponds, landfills, and excavation sites—has expanded due to the ability to quickly collect detailed spatial data. The high density of points, typically ranging from 200 to over 1000 points per square meter, enables the creation of detailed Digital Terrain Models (DTMs) that serve as a basis for volumetric calculations.

Several studies [6-10] have addressed the accuracy of volume estimates based on LiDAR-derived models. For instance, Hodgson and Bresnahan (2004) evaluated vertical accuracy across different land cover types and concluded that RMSE in elevation can vary from 15 cm in open areas to more than 50 cm in vegetated regions. Despite these challenges, LiDAR remains one of the most reliable methods for terrain documentation, especially when validated with Ground Control Points (GCPs).

Error estimation techniques, including the use of statistical analysis and field validation, are key to assessing the reliability of LiDAR-based 3D models. Commonly used accuracy metrics include Root Mean Square Error (RMSE), standard deviation, and absolute mean error. Shifts in horizontal or vertical positioning due to calibration errors, vegetation interference, or GNSS inaccuracies may significantly affect derived volumes.

Recent case studies demonstrate how LiDAR-based measurements support earth mass balance evaluations and post-operational monitoring of tailing ponds and mining areas. The possibility to compare successive scans over time allows engineers to track terrain deformation, subsidence, or accumulation with high confidence. For example, González-Aguilera et al. (2012) [11]applied airborne LiDAR to monitor volumetric changes in a landfill, achieving sub-meter accuracy with refined post-processing.

Post-processing of data acquired through LiDAR technology is a crucial step in transforming raw point cloud datasets into meaningful and actionable information. Specialized software such as DJI Terra and Terrasolid are widely used for this purpose, offering advanced functionalities not only to generate high-resolution 3D terrain models, but also to classify point clouds into specific categories. These include extracting the ground surface (Ground class), identifying built-up areas, and mapping vegetation cover, often down to specific plant types using machine learning and artificial intelligence algorithms. This classification enhances the usability of the dataset in environmental monitoring, land management, and infrastructure planning.

However, it is important to highlight that such advanced applications demand dedicated computing infrastructure due to the large volume of data involved in LiDAR processing. Creating a detailed 3D model of a large area using standard consumer hardware can result in extremely long processing times. Therefore, having access to a high-performance workstation—equipped with a powerful graphics processing unit (GPU), high-speed RAM, and fast solid-state drives (SSD)—is essential for efficient and accurate LiDAR data post-processing. These hardware specifications significantly reduce processing time and ensure the seamless handling of complex datasets.

2. Materials and Methods

The research object selected for analysis, presented at Fig.1, was a facility used for storing post-flotation waste from secondary zinc ore processing. The storage site was established in the 20th century during the operation of zinc and lead ore mines located near the town of Olkusz. Mining operations in the area ceased in the early 2020s. Advances in zinc and lead ore processing technologies have made it economically feasible to reprocess the previously deposited waste material. This approach offers not only economic benefits but also environmental advantages, as it allows for the recovery of significant quantities of zinc and lead without the need for new extraction activities.

Fig. 1: Location of the research site – post-flotation sedimentation ponds in Bukowno (Southern Poland)

The surface area of the deposited post-flotation sediments amounts to 137 hectares. The elevation difference between the base of the stockpile and the legally permitted final elevation is 50 meters. The sedimentation ponds are constructed in 5-meter-high segments, with the protective embankment built at a 1:3 slope.

At every 5-meter height increment, a horizontal bench is formed, typically used for access roads or the installation of drainage systems. The facility is regularly monitored in terms of structural stability, groundwater levels, and the quality of water used in the closed-loop system.

It is essential that the management of the company operating the sedimentation ponds has accurate and up-to-date information on the quantity of post-flotation sediments previously deposited, which can now be reprocessed. To estimate these volumes, the use of the LIDAR L2 technology was proposed, assuming both a high level of spatial accuracy in 3D modeling (due to relatively low vegetation cover) and an efficient data processing workflow.

To carry out the field measurements, post-processing, and analysis of the obtained data, the following equipment and software were used:

- DJI Zenmuse L2 LiDAR sensor mounted on an unmanned aerial vehicle (UAV) DJI Matrice 350 RTK (Figure 2). The system is equipped with a high-frequency precision laser and integrated GNSS (Global Navigation Satellite System) and IMU (Inertial Measurement Unit) modules, allowing the acquisition of dense and accurate 3D point clouds. It offers high measurement accuracy—typically up to 4 cm vertically and 5 cm horizontally—and performs efficiently in various terrain conditions. The accuracy may improve further in areas with minimal vegetation, provided it is confirmed by independent geodetic measurements using certified equipment.
- Topcon HiPer XR GNSS receiver with dual-constellation and dual-frequency capabilities, supporting GPS and GLONASS signals, which significantly enhances positional accuracy even in challenging field conditions. Its integrated radio and cellular communication allow for seamless Real-Time Kinematic (RTK) corrections, enabling horizontal accuracy of approximately ±5 mm and vertical accuracy of approximately ±10 mm under optimal conditions. The receiver was used for collecting control points that served as ground truth in the verification of 3D terrain models generated from LiDAR data, contributing to the assessment of both horizontal and vertical accuracy,
- QGIS (version 3.30.0) for processing geodetic measurement data,
- RStudio (version 2025.05.1) for statistical analysis used to evaluate the accuracy of the 3D model reconstruction.

Fig. 2: DJI MATRICE 350 RTK drone equipped with the GJI ZENMUSE L2 LIDAR sensor during the survey of the research site on July 10, 2025

Laser scanning of the research site was carried out according to the flight scheme shown in Figure 3. The surveyed area covered 146.2 hectares, which exceeded the actual surface area of the object in order to ensure complete coverage and accurate representation in the 3D model

Fig. 3. Survey area using the LIDAR head with flight trajectories and take-off points of the DJI MATRICE 350 RTK drone.

Additionally, geodetic measurements were carried out using the Topcon HiPer XR receiver to determine the coordinates of characteristic points for evaluating the accuracy of horizontal coordinate representation in the 3D model. These points were marked with red targets, which were simultaneously documented in photographs taken during the laser scanning process by the LIDAR head. The locations of the reference points are shown in Figure 4.

Fig. 4. Location of control points used to assess the accuracy of horizontal geodetic coordinate representation in the 3D model (coordinate system: EPSG:2178)

For the purpose of estimating the error in representing geodetic elevations in the 3D model, measurements of 46 control points were carried out using the Topcon HiPer XR geodetic receiver. The location of these points is shown in Figure 5.

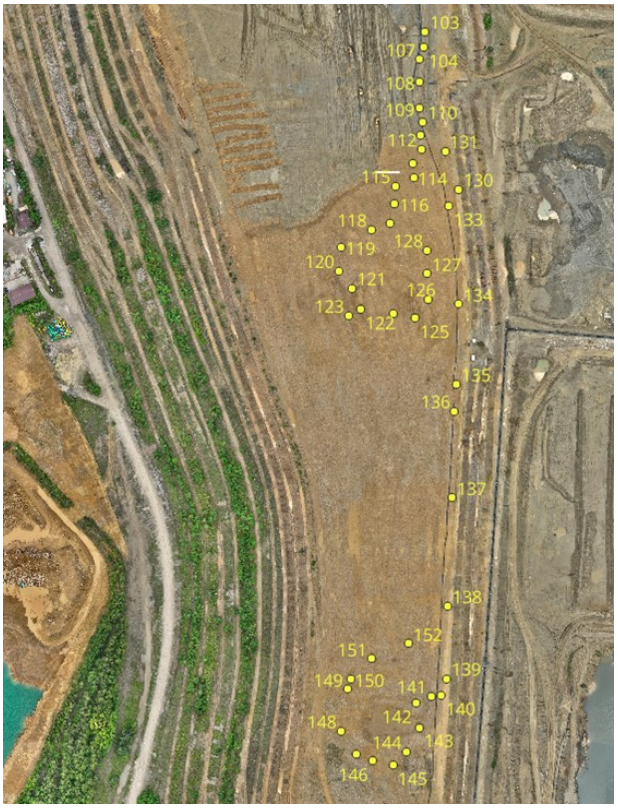

Fig. 5. Location of control points used to assess the accuracy of geodetic elevation representation in the 3D model (coordinate system compliant with EPSG:2178, PL-EVRF2007-NH geoid)

All measurement results were recorded on the electronic storage devices of the respective equipment controllers. The laser scanning of the study area and adjacent zones, as indicated in Figure 3, generated 32.6 GB of data. The resulting point cloud was initially saved with horizontal coordinates in the WGS 84/UTM Zone 34 reference system and with vertical coordinates based on the ellipsoidal height system. During the data post-processing phase, these coordinates were transformed into the official reference system EPSG:2178 and the PL-EVRF2007-NH geoid.

For the purpose of statistical analysis of the geodetic measurement data and values obtained from the 3D model, commonly used descriptive statistics were employed, along with the Shapiro–Wilk normality test and Tukey's outlier detection method.

The Shapiro–Wilk test is a statistical test used to assess whether a data sample follows a normal (Gaussian) distribution. The null hypothesis of the test assumes normality. If the resulting p-value is greater than a chosen significance level (commonly 0.05), the null hypothesis cannot be rejected, indicating that the data is likely normally distributed 12].

The Tukey's fences method [12] is used to identify outliers in a dataset. It is based on the interquartile range (IQR) and determines lower and upper thresholds beyond which values are considered outliers:

- Lower Fence = Q1 − k × IQR
- Upper Fence = Q3 + k × IQR

where Q1 and Q3 are the first and third quartiles, respectively, and k is a constant typically set to 1.5. Values outside this range are flagged as potential outliers.

The main descriptive statistics calculated during the analysis include:

- Mean (average) – the central tendency of the data
- Median – the middle value, useful in the presence of outliers
- Standard deviation (S) – a measure of the dispersion of data values around the mean
- Skewness – an indicator of the symmetry of the distribution
- Kurtosis – describes the tail behavior of the distribution
- Minimum and maximum values – defining the range of the dataset.

These methods collectively provide a comprehensive insight into the accuracy and reliability of the spatial data, including the presence of anomalies and the distribution characteristics of the measured values.

2.1 Postprocessing of LIDAR Data

DJI Terra software was used for processing the data collected during UAV-based LIDAR surveys conducted with systems such as the Zenmuse L2 sensor. The software enables comprehensive point cloud postprocessing, including classification (e.g., distinguishing between ground, vegetation, and infrastructure), noise filtering, generation of DTM (Digital Terrain Model) and DSM (Digital Surface Model), as well as export to common formats such as LAS or DXF. DJI Terra also supports the automatic generation of orthophotos and 3D models. The program integrates data from GNSS (Global Navigation Satellite System) and IMU (Inertial Measurement Unit), ensuring accurate georeferencing of results.

The LIDAR data processed in DJI Terra provides highly detailed and dense point clouds—typically ranging from 200 to over 1000 points per square meter, depending on flight height, UAV speed, and surface conditions. This high resolution allows for precise representation of terrain, vegetation, and built structures. The density of points significantly improves the accuracy of DTM models, which is particularly important in earthwork volume analyses.

However, the final accuracy may be affected by several factors, such as errors in GNSS/IMU data integration, atmospheric interference, signal reflection from irregular surfaces (e.g., water, glass), or poor sensor calibration. To mitigate such issues, DJI Terra includes tools for point filtering, classification, and manual editing, which help reduce both systematic and random errors. In practice, under favorable measurement conditions, the models generated by DJI Terra can achieve accuracies within a few centimeters.

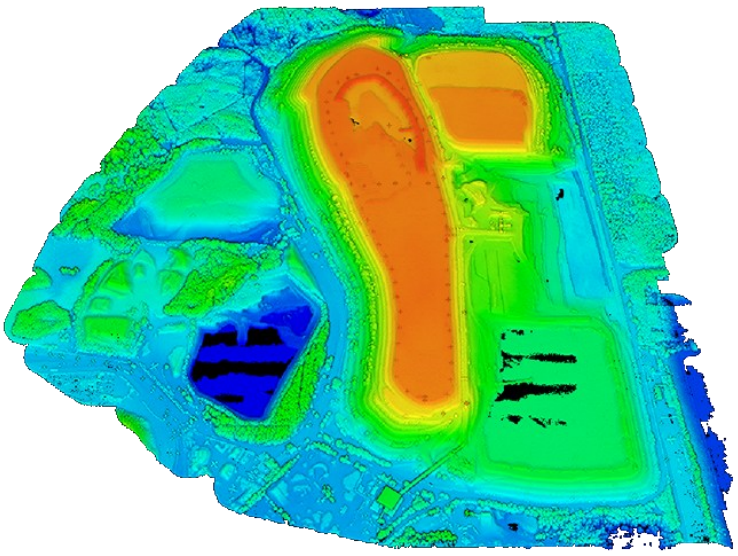

Fig. 6. 3D model of the research object and surrounding area in the form of a point cloud generated using DJI Terra software.

An important aspect of LIDAR data processing in DJI Terra is the time required for computations. This depends on various factors including the size of the dataset, terrain complexity, processing parameters, and the computer's processing power. For typical missions lasting 15–20 minutes, point cloud and terrain model generation may take from 30 minutes to several hours. This process

includes GNSS/IMU data synchronization, flight path reconstruction, point classification, and digital model generation. High-performance computers with dedicated GPUs greatly reduce processing time. Therefore, using systems that meet or exceed DJI Terra's hardware recommendations is strongly advised—especially when analyzing large areas or producing high-resolution models.

In the case of scanning the sedimentation pond site, five separate flight missions, each lasting approximately 30 minutes, were conducted. The time required to generate a point cloud at a density of 50 pts/m² using a computer equipped with an Intel Core i7 processor was around 10 hours. Figure 6 presents the full point cloud generated by DJI Terra for the scanned area. The resulting 3D model of the sedimentation ponds was exported in standard geospatial formats compatible with GIS platforms, such as QGIS 3.30.0. Further data analysis and visualization were carried out using QGIS functionalities.

2.2 Accuracy Assessment of the 3D Model

As previously mentioned, to assess the accuracy of the 3D model generated from the LIDAR survey, independent geodetic measurements of control points were conducted. For the evaluation of horizontal coordinates (Δx, Δy), a total of 10 control points were measured, while for the assessment of elevation accuracy (Δz), measurements were performed at 46 control points.

The collected measurement data are presented in two tables (Table 1 and Table 3). Based on this data, differences were calculated between the coordinates derived from the 3D model and those obtained from geodetic field measurements.

Statistical analysis was performed on the sets of differences, including the identification of outliers using Tukey's test. Subsequently, basic descriptive statistics were calculated, including the mean, median, standard deviation, minimum, and maximum values. These measures enabled a detailed assessment of the spatial accuracy of the 3D model representation.

Tab. 1. Summary of the coordinates of control points used to assess the accuracy of the representation of horizontal geodetic coordinates in the 3D model (Coordinate reference system compliant with EPSG: 2178)

Point No.	Coordinates from 3D model		Coordinates from field survey		Differences	
	X [m]	Y [m]	X [m]	Y [m]	Δx [m]	Δy [m]
101	7392865.375	5573084.204	7392865.371	5573084.208	0.004	-0.004
102	7392872.440	5573134.361	7392872.434	5573134.320	0.006	0.041
109	7392870.276	5573060.595	7392870.222	5573060.606	0.054	-0.011
112	7392872.735	5573022.518	7392872.758	5573022.555	-0.023	-0.037
115	7392848.328	5572988.700	7392848.349	5572988.641	-0.021	0.059
118	7392825.970	5572948.186	7392825.964	5572948.186	0.006	0.000
119	7392797.946	5572932.407	7392797.952	5572932.353	-0.006	0.054
123	7392804.884	5572868.610	7392804.852	5572868.669	0.032	-0.059
129	7392896.457	5572967.787	7392896.314	5572967.677	0.143	0.110
132	7392900.351	5573036.717	7392900.352	5573036.663	-0.001	0.054

2.3 Tukey's Fence and Shapiro-Wilk Tests Results for Δx ,Δy and Δz

For the dataset containing 10 observations of Δx values, an outlier detection analysis was performed using Tukey's fences method. Based on the dataset, the following quartile values were calculated:

- **First quartile (Q1)** = –0.006
- **Third quartile (Q3)** = 0.032
- **Interquartile range (IQR)** = Q3 – Q1 = 0.038

From these, the lower and upper bounds for identifying potential outliers were established:

- **Lower bound**: Q1 – 1.5 × IQR = –0.063
- **Upper bound**: Q3 + 1.5 × IQR = 0.089

Any value falling outside this range was classified as an outlier. The analysis identified one such outlier: **0.143**, which exceeded the upper threshold. All other values fell within the defined range and were not considered outliers. This outlier may significantly affect the statistical calculations and is therefore recommended to be excluded from further descriptive statistical analysis, particularly if the analysis is intended to characterize a typical (unperturbed) distribution.

For **Δy**, the following quartile values were obtained:

- First quartile (Q1) = –0.011
- Third quartile (Q3) = 0.054
- Interquartile range (IQR) = Q3 – Q1 = 0.065

Based on these, the boundaries for detecting outliers were defined as:

- Lower bound: Q1 – 1.5 × IQR = –0.1085
- Upper bound: Q3 + 1.5 × IQR = 0.1515

Upon comparison of all values in the Δy dataset with these thresholds, it was found that **no values exceeded** the established bounds. Therefore, the Δy dataset contains **no outliers** according to the Tukey's fence test. The data can be considered homogeneous and suitable for further statistical analysis without modification.

Due to the outlier detected in Δx for **Point No. 129**, it was excluded from the subsequent statistical analysis.

For the revised dataset from **Table 1**, excluding Point 129, a statistical normality test was carried out to verify whether the Δx and Δy sequences follow a normal distribution, i.e., whether the horizontal coordinate errors exhibit random behavior. For this purpose, the widely recognized **Shapiro–Wilk test** was used.

The Shapiro–Wilk test is a statistical test of normality used to assess whether the distribution of a continuous variable conforms to a normal distribution. It is one of the most commonly used tests in statistical analysis due to its high sensitivity, especially for small sample sizes. In practice, the test compares the empirical values with the expected values under the assumption of normality by calculating the W statistic. The closer the W statistic is to 1, the greater the probability that the data come from a normal distribution.

Tab. 2. Descriptive Statistics and Shapiro–Wilk Test Results for the Δx and Δy Series

Parameter	Δx [m]	Δy [m]
P-value	0.3029	0.281
W statistic	0.9058	0.9026
Number of observations (n)	9	9
Mean ($\bar{x}$)	0.0057	0.0108
Median	0.004	0
Standard deviation (S)	0.0244	0.0432
Sum of squares	0.0047	0.0149
Population variance (b)	0.0656	0.1161
Skewness	0.965	-0.3235
Skewness shape	Symmetrical	Symmetrical
Excess kurtosis	0.8625	-1.3111
Kurtosis shape	Normal	Normal
Outliers	None	None

The Shapiro–Wilk test plays an important role in engineering and geodetic analyses because many statistical methods (e.g., parametric tests, estimators, or error analysis) assume the normality of the data distribution. Assessing normality allows the selection of appropriate methods for further analysis: parametric (if the distribution is normal) or non-parametric (if the distribution deviates from normality). Therefore, the Shapiro–Wilk test is a crucial step in validating the accuracy of measurement results and the quality of numerical models, such as in the accuracy assessment of LiDAR data.

Below is the interpretation of the Shapiro–Wilk test results for the Δx and Δy datasets. A p-value greater than 0.05 indicates no reason to reject the null hypothesis of normality. In addition to the Shapiro–Wilk test, basic descriptive statistics, skewness, kurtosis, and the presence of outliers were also analyzed.

For both data series – Δx and Δy – the p-values are 0.3029 and 0.281 respectively, which means that for both cases, there is no reason to reject the null hypothesis of normal distribution. This implies that both distributions can be considered normally distributed.

The descriptive statistics show that the mean and median values are close, which also indicates a symmetric distribution. The skewness index for Δx (0.965) suggests a slightly right-skewed distribution, and for Δy (–0.3235) – a slight left-skewness; however, in both cases, the values are not significant enough to classify the distributions as asymmetrical. Kurtosis is positive for Δx and negative for Δy, indicating minor differences in "peakedness" relative to the normal distribution, but these do not significantly affect the overall assessment.

In summary, both data series can be treated as normally distributed, allowing the application of statistical methods based on the normal distribution.

To accurately estimate the error in horizontal coordinate mapping based on measurement data, it is necessary to analyze the absolute values of the coordinate differences Δx and Δy. This is because if the differences contain both positive and negative values, their arithmetic mean may approach zero, potentially leading to incorrect conclusions about high measurement accuracy. In practice, these errors occur regardless of sign, and their true impact on accuracy should be assessed based on absolute deviations.

Tab. 3. Descriptive Statistics for the Δx and Δy Series (Based on Absolute Values)

Parameter	Δx [m]	Δy [m]
Mean ($\bar{x}$)	0.017	0.036
Median	0.006	0.041
Standard deviation (S)	0.017	0.024

For the data presented in Table 3, the mean, median, and standard deviation values were calculated based on the absolute differences. The average absolute difference in the x-direction (Δx) is 0.017, while in the y-direction (Δy) it is slightly higher, reaching 0.036. The median values of the differences indicate that half of the observed errors are below 0.006 (for Δx) and 0.041 (for Δy), which further confirms the relatively low dispersion. The standard deviation, as a measure of variability, indicates slightly higher instability in the y-direction.

In summary, using absolute values in the analysis of coordinate errors is essential for reliable estimation of the spatial model accuracy and for avoiding misinterpretations caused by potential cancellation of errors with opposite signs.

Similar analyses were performed for the dataset used to assess the accuracy of the vertical coordinates (Δz) based on the PL-EVRF2007-NH geoid (Table 4). To compare the values from the model and field measurements, the vertical values (elevations) of the surveyed points with horizontal coordinates listed in Table 4 were assigned values extracted from the 3D model using the QGIS software. In QGIS, the ***Sample Raster Values*** tool is implemented to assign raster values (e.g., elevation, temperature, humidity) to points in a vector layer. This functionality is particularly useful in spatial analysis where it is necessary to retrieve raster values at specific locations, such as GPS coordinates. The tool creates a new column in the attribute table of the points, containing sampled values from one or more rasters, enabling further statistical and spatial analysis. The Z-values in the '3D Model' column in Table 4 were obtained using the aforementioned function.

Tukey's test for outliers was applied to the Δz dataset, utilizing the interquartile range (IQR) method. The first quartile (Q1) was calculated to be -0.012, and the third quartile (Q3) was 0.017, resulting in an IQR of:

$$IQR = Q3 - Q1 = 0.017 - (-0.012) = 0.029$$

Based on this, the acceptable data range was defined as follows:

Lower bound: $Q1 - 1.5 \times IQR = -0.012 - 1.5 \times 0.029 = -0.0555$

Upper bound: $Q3 + 1.5 \times IQR = 0.017 + 1.5 \times 0.029 = 0.0605$

With a sample size of n = 46, Tukey's test identified no outliers, indicating that all Δz values fall within the acceptable range between -0.0555 and 0.0605. Therefore, these data can be considered statistically consistent and suitable for further analysis without the need to exclude any outlying observations.

Tab. 4. Set of control point coordinates used to assess the accuracy of geodetic elevation representation in the 3D model (coordinate reference system compliant with EPSG: 2178, PL-EVRF2007-NH geoid)

Point No.	Coordinates from field survey			3D Model Z [m a.s.l]	Differences Δz [m]
	Y [m]	X [m]	Z [m a.s.l]		
103	5573131.999	7392875.992	373.559	373.563	-0.004
104	5573117.408	7392874.666	373.773	373.754	0.019
107	5573106.090	7392871.037	373.867	373.852	0.015
108	5573085.202	7392870.818	374.634	374.602	0.032
109	5573060.606	7392870.222	373.488	373.451	0.037
110	5573047.922	7392873.976	372.236	372.207	0.029
111	5573035.922	7392871.279	370.682	370.688	-0.006
112	5573022.555	7392872.758	370.368	370.351	0.017
113	5573009.264	7392864.189	370.309	370.347	-0.038
114	5572996.744	7392865.201	370.152	370.161	-0.009
115	5572988.641	7392848.349	370.174	370.148	0.026
116	5572972.481	7392847.678	370.200	370.212	-0.012
117	5572954.843	7392843.955	370.132	370.135	-0.003
118	5572948.186	7392825.964	370.127	370.110	0.017
119	5572932.353	7392797.952	370.154	370.127	0.027
120	5572910.081	7392796.370	370.034	370.042	-0.008
121	5572894.019	7392808.325	370.034	370.026	0.008
122	5572874.888	7392816.060	369.957	370.003	-0.046
123	5572868.669	7392804.852	369.945	369.992	-0.047
124	5572871.114	7392846.737	370.180	370.194	-0.014
125	5572866.418	7392866.625	370.226	370.260	-0.034
126	5572883.921	7392878.839	370.122	370.106	0.016
127	5572907.670	7392877.835	370.076	370.066	0.010
128	5572929.303	7392878.015	370.007	370.016	-0.009
130	5572985.450	7392907.172	370.077	370.091	-0.014
131	5573020.988	7392894.382	370.185	370.164	0.021
133	5572970.676	7392897.896	370.052	370.032	0.020
134	5572879.478	7392907.326	370.130	370.135	-0.005
135	5572805.101	7392905.002	370.471	370.502	-0.031
136	5572780.338	7392903.315	370.173	370.177	-0.004
137	5572700.268	7392900.987	370.590	370.586	0.004
138	5572599.697	7392896.717	370.754	370.741	0.013
139	5572532.759	7392895.925	370.720	370.726	-0.006
140	5572517.631	7392890.723	370.527	370.527	0.000
141	5572516.297	7392881.645	370.239	370.241	-0.002
142	5572510.449	7392867.357	370.179	370.198	-0.019
143	5572487.626	7392870.971	370.003	370.045	-0.042
144	5572465.393	7392858.629	370.221	370.215	0.006
145	5572453.085	7392846.261	370.241	370.243	-0.002
146	5572456.728	7392826.990	370.277	370.288	-0.011
147	5572463.486	7392812.743	370.272	370.250	0.022
148	5572484.007	7392798.424	370.292	370.282	0.010
149	5572522.969	7392803.857	370.344	370.363	-0.019
150	5572532.386	7392806.823	370.320	370.341	-0.021
151	5572551.160	7392826.076	370.534	370.522	0.012
152	5572565.217	7392860.340	370.435	370.402	0.033

Tab. 5. Results of the Shapiro–Wilk Test for the Δz Series

Parameter	Value
p-value	0.1016
Shapiro–Wilk statistic (W)	0.9587
Sample size (n)	46
Mean ($\bar{x}$)	–0.00026
Median	–0.002
Standard deviation (S)	0.02157
Sum of squares	0.02094
Coefficient b	0.1417
Skewness	–0.4102
Skewness interpretation	Potentially symmetrical distribution (p = 0.241)
Excess kurtosis	–0.386
Kurtosis interpretation	Potentially mesokurtic – normal-like distribution (p = 0.575)

Results of the Shapiro–Wilk Test for the Δz Series are presentet in Table 5. The p-value of the Shapiro–Wilk test was 0.1016, which indicates that at the standard significance level of $\alpha = 0.05$, there is no basis for rejecting the null hypothesis of normality. This means that the distribution of the Δz dataset can be considered consistent with a normal distribution.

Additionally, the W statistic value (0.9587) falls within the acceptable range for normally distributed data, and both the skewness (–0.4102) and excess kurtosis (–0.386) parameters confirm the absence of significant deviations from normality. The distribution is slightly left-skewed but remains symmetrical and mesokurtic (i.e., it exhibits tails similar to the normal distribution).

No outliers were detected in the analysis. Therefore, the dataset can be considered internally consistent and reliable for further statistical analysis under the assumption of normality.

Tab. 6. Descriptive Statistics for the Δz serie (Based on Absolute Values)

Parameter	Δz [m]
Mean ($\bar{x}$)	0.017
Median	0.015
Standard deviation (S)	0.013

The mean, median, and standard deviation values presented in Table 6 were calculated based on the absolute values of the elevation differences. The mean absolute elevation difference is 0.017 m. The median value of the dataset is 0.015 m, which is very close to the arithmetic mean. This small difference between the median and mean suggests a symmetrical distribution with no significant outliers. The standard deviation (S) = 0.013 m indicates a low variability of Δz values around the mean.

In practice, this means that most measurement differences fall within the ±1.3 cm range, which confirms the high accuracy of the elevation data.

The statistical values indicate very high data quality – the small mean deviation and low variability suggest that the 3D model has been reproduced with high accuracy. This level of error is acceptable, and even considered excellent, in engineering-grade geodetic and environmental analyses.

2.4 Volume estimation of stockpiles

In order to obtain an accurate measurement of the volume of post-flotation tailings deposited within the sedimentation ponds, a geodetic analysis was conducted. This analysis was based on data obtained from airborne LiDAR scanning.

A section corresponding to the spatial extent of the sedimentation ponds was extracted from the total scanned area (illustrated in Figure 5). The selection of this area was driven by the objective of accurately reflecting the boundaries of the hydrotechnical structures utilized for the deposition of flotation waste.

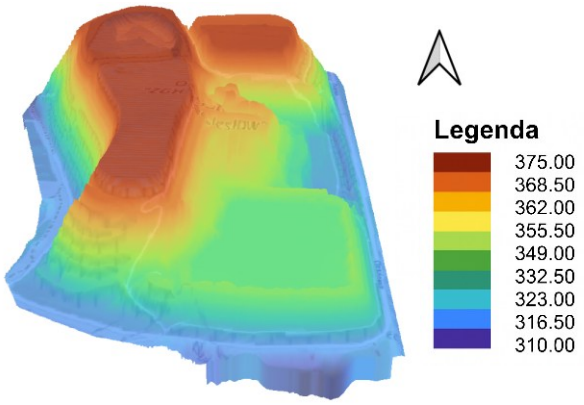

Fig. 7. Overview view from the south side of the 3D model of the study object used to analyze the masses of deposited sediments

Figures 7 presents a three-dimensional model of the extracted area, along with an elevation interpretation. The base level of the sedimentation ponds was assumed to be located at 320.00 meters above sea level. Consequently, all terrain volumes situated above this elevation are interpreted as material deposited during the operation of the tailings ponds.

The selection of the spatial extent for analysis was made with the consideration of the necessity to eliminate the influence of adjacent structures and surrounding terrain. This helped minimize the risk of overestimating the volume due to unaccounted earth masses beyond the designated deposition area. This methodology enabled a reliable estimation of the volume of material located above the reference level, thereby facilitating an accurate assessment of the quantity of accumulated post-flotation tailings.

In order to conduct a precise analysis of the volume of deposited post-flotation sediments, the research site was divided into sub-areas (Fig. 8). The basic division was based on the distinction between two main units: the Western pond and the Eastern pond.

Due to the varied use and degree of filling, the Eastern pond was further divided into three functional sections, in accordance with the current state of development of the facility.

- the north-eastern section covers the area where the process of depositing post-flotation sediments has already been completed. This area is currently unused and may be subject to stability assessment and possible reclamation.
- the central section is the currently exploited part of the pond, where secondary flotation is carried out. It is a dynamically used part of the facility, requiring ongoing monitoring of the amount of deposited soil.
- the south-eastern section is intended for the deposition of sludge produced after the secondary flotation process. This area is characterised by a different composition of the stored material, which may be relevant for further technical and environmental analyses.

This approach to the division of sedimentation ponds allows for a detailed analysis of the spatial distribution of sediments, which is important when planning further stages of operation and assessing the load-bearing capacity and stability of individual sections of the landfill. In addition, by separating the sections corresponding to the phases of operation.

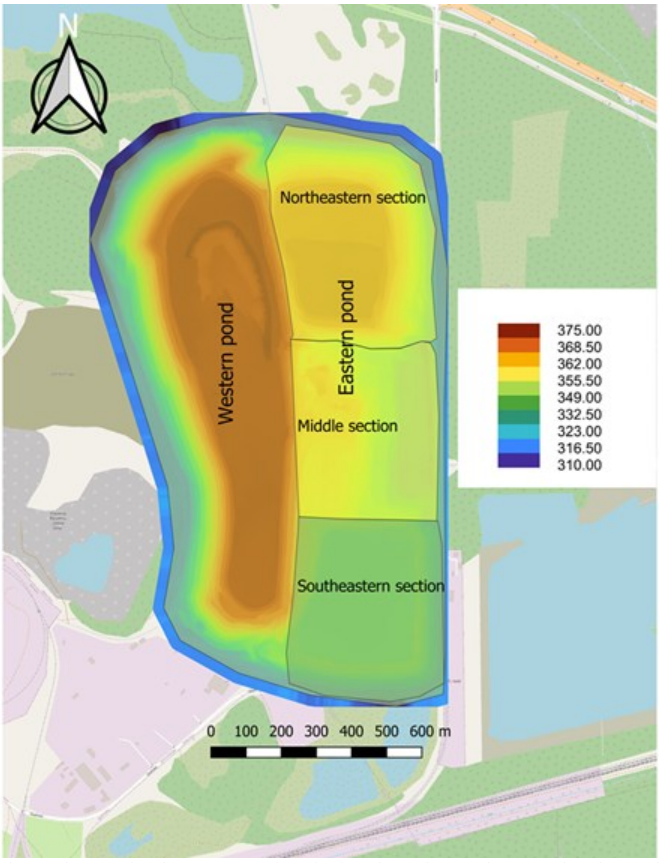

Fig. 8. Division of the study area for the purpose of analyzing the volume of accumulated post-flotation sediments.

A summary of the volumes and areas of individual elements of the sediment ponds, assuming a foundation level of 320.00 m above sea level, is presented in Table 7.

Tab. 6. Summary of the volume and area of sedimentation ponds as of July 10, 2025

Element	Volume [mln m^3]	Area [ha]
Total sedimentation ponds	37.488	137.879
Western Pond	21.442	71.061
Eastern Pond	16.047	66.817
Northeastern section of the Eastern Pond	8.765	25.042
Central section of the Eastern Pond	4.038	20.362
Southeastern section of the Eastern Pond	3.244	21.413

The generated 3D model of the sedimentation facility enables precise estimation of the volume of post-flotation tailings stored within the area, based on terrain elevation data, as illustrated in Figure 9. This high-resolution volumetric analysis allows for the differentiation of material accumulation across various segments of the site, providing a valuable spatial overview of the deposition process. Such detailed information empowers the facility operator to monitor the quantity of deposited material in individual zones,

which is essential for effective resource planning, ongoing operational control, and environmental management. Moreover, the model supports strategic decision-making related to future land reclamation, capacity assessments, and regulatory compliance, making it a critical tool for both production optimization and sustainable tailings management.

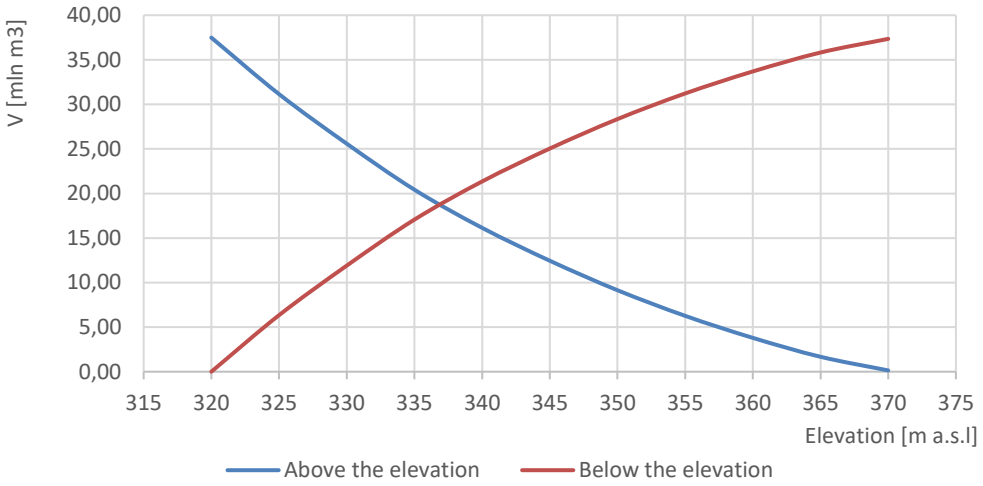

Fig. 9. Chart showing the total volume of sedimentary deposits as of July 10, 2025.

3. Conclusion

The findings of this study confirm that drone-based LiDAR scanning, supported by precision GNSS validation, provides a robust and efficient method for volumetric assessment of large-scale industrial tailings ponds. The achieved spatial resolution—up to 50 pts/m²—and sub-decimeter accuracy are sufficient for high-precision geodetic and environmental monitoring, aligning with previous research by MacDonell et al. (2023)[4], who demonstrated similar levels of accuracy in vegetated riverine terrains. Furthermore, the ability to distinguish between different operational zones within the ponds facilitates targeted environmental management and future reclamation planning.

When compared to airborne laser scanning (ALS) systems, such as those studied by Resop et al. (2019)[5], UAV-LiDAR offers superior flexibility and spatial granularity at low altitudes. This study also supports previous conclusions by Glennie et al. (2013) [1], Wallace et al. (2012) [2] and Li et al.(2013) [13], which emphasize the advantages of trajectory and scanner integration in ensuring geodetic reliability. The integration of semi-automated processing tools and geostatistical methods further enhances the applicability of UAV-LiDAR systems in operational mining and environmental contexts.

In conclusion, the presented methodology demonstrates that consumer-grade drone-mounted LiDAR systems, when coupled with systematic field validation and robust post-processing, can serve as a cost-effective and scalable solution for volumetric monitoring in post-industrial landscapes.

References

1. Glennie, C.L., et al. (2013). Geodetic imaging using airborne LiDAR: The benefits of scanner and trajectory data integration. Journal of Surveying Engineering, 139(4), 183–192.
2. Wallace, L., Lucieer, A., Watson, C. (2012). Evaluating tree detection and segmentation routines on very high resolution UAV LiDAR data. IEEE Transactions on Geoscience and Remote Sensing, 50(2), 712–726.
3. Stoker, J.M.; Abdullah, Q.A.; Nayegandhi, A.; Winehouse, J. Evaluation of single photon and Geiger mode LiDAR for the 3D elevation program. Remote Sens. 2016, 8, 767
4. MacDonell, R., et al. (2023). Consumer-grade UAV solid-state LiDAR accurately quantifies topography in a fluvial environment. Earth Surface Processes and Landforms.
5. Resop, J. P., Lehmann, L., & Hession, W. C. (2019). Drone Laser Scanning for Modeling Riverscape Topography and Vegetation: Comparison with Traditional Aerial Lidar. Drones, 3(2), 35. https://doi.org/10.3390/drones3020035
6. Whitehead, K., Hugenholtz, C.H. (2014). Remote sensing of the environment with small unmanned aircraft systems (UASs), part 1: A review of progress and challenges. Journal of Unmanned Vehicle Systems, 2(3), 69–85.
7. Wróżyński, R., Pyszny, K., & Sojka, M. (2020). Quantitative Landscape Assessment Using LiDAR and Rendered 360° Panoramic Images. Remote Sensing, 12(3), 386.
8. Hohenthal, J., Alho, P., Hyyppä, J., Hyyppä, H. (2011). Laser scanning applications in fluvial studies. Progress in Physical Geography, 35(6), 782–809.
9. Kasvi, E., et al. (2015). Monitoring fluvial processes with UAV-based photogrammetric and field survey data: A study of point bar evolution in the River Tenojoki, Finland. Geomorphology, 238, 306–321.
10. James, M.R., Quinton, J.N. (2014). Accuracy and precision of photogrammetric ground control points for UAV-derived 3-D models. Earth Surface Processes and Landforms, 39(9), 1055–1062.
11. González-Aguilera, D., Gómez-Lahoz, J., Rodríguez-Gonzálvez, P., & Herrero-Pascual, J. (2012). Monitoring landfill volume changes using a terrestrial laser scanner. Measurement, 45(2), 354–360.
12. E. Pebesma, "Simple Features for R: Standardized Support for Spatial Vector Data," in The R Journal, edited by (R NEWS, 2018), pp. 439–446. doi:10.32614/RJ-2018-009
13. Li, Huxiong & Ye, Weiya & Liu, Jun & Tan, Weikai & Pirasteh, Saied & Fatholahi, Sarah Narges & Li, Jonathan. (2021). Remote sensing High-Resolution Terrain Modeling Using Airborne LiDAR Data with Transfer Learning. Remote Sensing. 13. 3448. 10.3390/rs13173448.